Land Cover and Vegetation Change Assessment after Extreme Precipitation Events: The Case of Tropical Storm Hanna (2020) in Northeastern Mexico Using Sentinel-2 and Random Forest

Luis Eduardo Arista-Cázares[1], Fabiola D. Yépez-Rincón[1], Kevin David Rodríguez-González[1], Nelly Lucero Ramírez-Serrato[2]

[1]Universidad Autónoma de Nuevo León, Civil Engineering Faculty, Department of Geomatics, San Nicolás de los Garza, Nuevo León, México – luis.aristaca@uanl.edu.mx ; fabiola.yepezrn@uanl.edu.mx ; krodriguezg96@gmail.com

[2]Universidad Nacional Autónoma de México, Natural Resources Department, Mexico City, México – nellyrmz@igeofisica.unam.mx

Keywords: post-disaster assessment, extreme precipitation, Sentinel-2A, random forest, Google Earth Engine (GEE), spectral indices.

Abstract

This study evaluates land cover responses to extreme rainfall in the Monterrey Metropolitan Area (Mexico) using Sentinel-2 imagery and remote sensing techniques. Two land cover maps were generated through Random Forest classification with stratified random sampling, considering six classes: dense vegetation, medium vegetation, sparse vegetation, built-up area, bare soil, and water bodies. Three spectral indices were incorporated: the Normalized Difference Vegetation Index (NDVI), the Soil Adjusted Vegetation Index (SAVI), and the Normalized Difference Water Index (NDWI). The pre- and post-event models achieved overall accuracies of 0.93 and 0.83, with Kappa coefficients of 0.91 and 0.79, respectively. Integration with a multi-index Change Vector Analysis (CVA) enabled the detection of both categorical and magnitude-based changes, revealing significant vegetation disturbance at higher elevations, vegetation recovery in mid-elevation zones, and increased surface moisture along riparian corridors after Tropical Storm Hanna (2020). These findings demonstrate the dual effects of extreme precipitation in semi-arid mountainous urban regions and highlight the value of combining vegetation and water indices for short-term change detection. The proposed methodology is transferable to other hazard-prone mountain cities worldwide, supporting disaster risk reduction, urban planning, and environmental monitoring. Limitations include the reliance on only two temporal scenes and spectral confusion between vegetation classes, which future studies could address through multi-temporal datasets, higher-resolution imagery, and integration of ancillary environmental data.

1. Introduction

Climate change has altered hydrological patterns worldwide, intensifying both rainfall events and prolonged droughts. The population of northeastern Mexico has been particularly affected by these contrasting phenomena within short temporal intervals, largely due to hydro-meteorological systems originating in the Atlantic Ocean and the Gulf of Mexico. These events, often associated with hurricanes that subsequently weaken into tropical storms, may still produce rainfall intensities exceeding those recorded during past extreme events (Touma et al., 2019). Such conditions have significant consequences for urban areas in the region, underscoring the need for holistic urban and environmental planning approaches that differ from the rest of the country (Froude and Petley, 2018; Pereira et al., 2020).

Within this context, the Monterrey Metropolitan Area (MMA)—commonly referred to as the "City of the Mountains" due to its rugged topography—stands out as one of the largest metropolitan areas in Latin America, and the second most important city in Mexico, with an estimated population of 5.3 million inhabitants (Secretaría de Desarrollo Agrario, Territorial y Urbano, SEDATU, 2024) which is a rapidly expanding urban region surrounded by steep mountainous terrain, which makes it highly vulnerable to extreme precipitation events. Tropical Storm Hanna, which struck on July 26, 2020, represents the most recent tropical cyclone to directly impact the region, producing intense rainfall and triggering widespread disturbances in vegetation and land cover.

This rapid urban growth has increased exposure and vulnerability to slope failures, often exacerbated by land use/land cover (LULC) changes or inadequate land management practices (Di Napoli et al., 2023; Pacheco Quevedo et al., 2023; Abdo and Richi, 2024).

Monitoring and quantifying these land surface changes is essential for urban planning and hazard mitigation and can be effectively achieved through remote sensing techniques at local, regional, and national scales, for example, by comparing two or more aerial or satellite images acquired over time (Isbaex & Coelho, 2021; Ansari et al., 2025).

Previous research has shown that land cover dynamics are influenced by both climatic drivers and anthropogenic pressures (Promper et al., 2014; Chen et al., 2019), and that these changes may significantly affect the likelihood of landslides in mountain urban regions. Understanding how extreme precipitation events influence vegetation and land cover conditions, and how these relate to slope instability, is therefore a critical research challenge in northeastern Mexico, where climatic extremes are recurrent.

This study addresses this gap by combining Sentinel-2 imagery, Random Forest (RF) land cover classification, vegetation and water indices: the Normalized Difference Vegetation Index (NDVI), the Soil Adjusted Vegetation Index (SAVI), and the Normalized Difference Water Index (NDWI), and a multi-index Change Vector Analysis (CVA) to evaluate land cover responses to Tropical Storm Hanna. The specific objectives are: (i) to classify pre- and post-event land cover and validate accuracy

with a confusion matrix; (ii) to quantify vegetation- and water-related changes through NDVI, SAVI, and NDWI; (iii) to apply a multi-index CVA to estimate the magnitude of spectral change; and (iv) to highlight the broader applicability of this methodological framework to other mountainous urban regions worldwide exposed to extreme rainfall events.

1.1 Study Area

The study area covers approximately 1,414 km² within the Monterrey Metropolitan Area (MMA), located in the state of Nuevo León, northeastern Mexico (Figure 1). The MMA currently comprises 13 municipalities: Monterrey, Guadalupe, San Nicolás de los Garza, San Pedro Garza García, General Escobedo, Santiago, Santa Catarina, García, El Carmen, Juárez, Cadereyta Jiménez, Apodaca, and Pesquería. However, the latter two municipalities are not included in this study due to their peripheral location and limited exposure to slope-related processes. The core of the MMA is situated within a tectonic depression surrounded by prominent mountain ranges belonging to the Sierra Madre Oriental, a morphotectonic province characterized by folded and thrusted sedimentary rocks formed during the Laramide orogeny (Padilla y Sánchez, 2007).

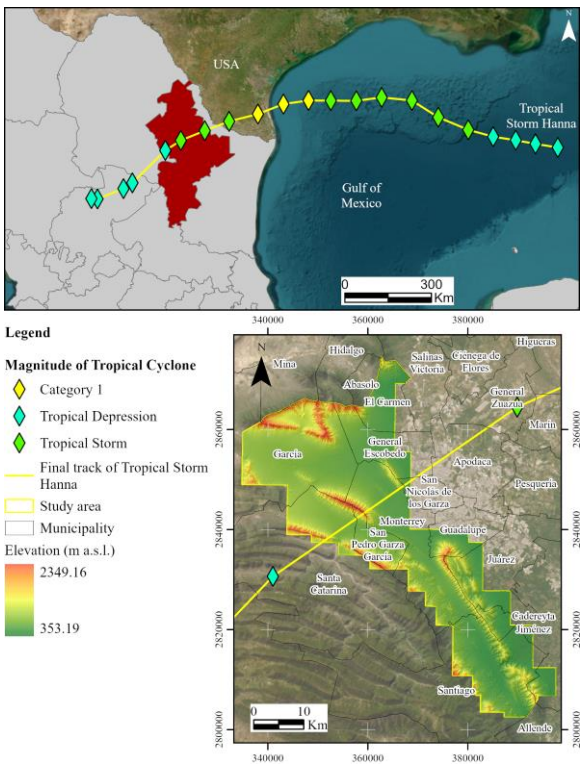

Figure 1. Location of the study area and track of Tropical Cyclone Hanna.

Elevation in the study area ranges from 353 m to 2,350 metres above sea level (m a.s.l.), creating strong topographic contrasts that directly influence hydrology, land use, and susceptibility to slope instability. Climatically, the MMA is located in a semi-arid to subtropical transitional zone, where rainfall is highly seasonal and concentrated during summer months (June–September). Average annual precipitation ranges between 500 and 900 mm; however, this balance is often disrupted by extreme tropical systems that generate localized but intense rainfall in short periods. Such events can surpass the regional hydrological capacity, resulting in flash floods, soil saturation, and slope failures.

In this context, Tropical Storm Hanna represents a relevant case study. Initially classified as a tropical depression in the Atlantic Ocean on July 22, 2020, Hanna intensified into a Category 1 hurricane on July 25 with sustained winds of 120 km/h, approximately 250 km northeast of Barra El Mezquital, Tamaulipas, Mexico. By July 26, the system weakened to a tropical storm as it tracked westward, directly crossing the Monterrey Metropolitan Area. According to the Mexican National Water Commission (Comisión Nacinal del Agua, CONAGUA, 2020), Hanna delivered maximum sustained winds of ~55 km/h and accumulated precipitation of up to 533 mm within the MMA.

Despite these hydrometeorological impacts in the region, coupled with past events (e.g., Hurricane Gilberto in 1988, Hurricane Alex in 2010, and Tropical Storm Ingrid in 2013), previous studies on land cover responses to extreme rainfall in northeastern Mexico are scarce (e.g., Yépez-Rincón et al., 2013; Aguilar Durán, 2017; Aguilar-Barajas et al., 2019).

2. Methodology

The methodological framework of this study is presented in Figure 2, integrating a sequential workflow to evaluate short-term land cover changes caused by Tropical Storm Hanna.

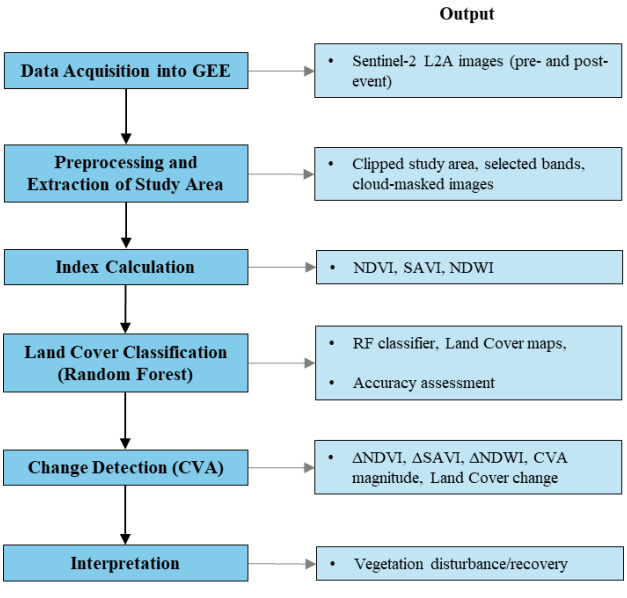

Figure 2. Flow chart of the adopted methodology based on Chrysafi et al. (2024) and Ansari et al. (2025).

2.1 Satellite imagery and preprocessing

Two cloud-free (<1% cloud cover) Sentinel-2 Level-2A multispectral images were acquired from the Copernicus Open Access Hub through Google Earth Engine (GEE). The selected scenes correspond to dates immediately before and after the landfall of Tropical Storm Hanna on 26 July 2020: July 13, 2020, and September 22, 2020, respectively, with a temporal gap of approximately one month to ensure minimal cloud contamination.

2.2 Vegetation and Water Indices

From the Sentinel-2 imagery, three spectral indices were calculated to assess post-event changes: NDVI to evaluate vegetation health, SAVI to reduce soil brightness effects, and NDWI to assess surface water content. These indices were selected because they jointly capture the most relevant biophysical responses to extreme rainfall-vegetation stress or recovery, soil-vegetation contrast in partially vegetated areas, and hydrological changes following heavy precipitation (Ansari et al., 2025). All indices were derived from Sentinel-2 spectral bands with a spatial resolution of 10 m (Table 1).

Sentinel-2A			
Bands	**Wavelenght (nm)**	**Bandwith (nm)**	**Spatial resolution (m)**
B3 – Green	559.8	36	10
B4 – Red	664.6	31	
B9 – Near-infrared	832.8	106	

Table 1. Sentinel-2A data.

2.2.1 Normalized Difference Vegetation Index (NDVI)

NDVI is one of the most widely used spectral indices to assess the state of vegetation health (Cabello et al., 2021; Zeng et al., 2024). It is obtained by the following equation (Rouse et al., 1974):

$$NDVI = \frac{NIR\ (B8) - Red\ (B4)}{NIR\ (B8) + Red\ (B4)} \quad (2)$$

The NDVI value varies between a range of -1 and +1, where positive values represent vegetation in good condition, while negative values or close to zero can indicate soil, artificial surfaces, or bodies of water.

2.2.2 Soil-Adjusted Vegetation Index (SAVI)

SAVI is an index proposed by Huete (1988), which is usually useful for detecting land cover when vegetation cover is scarce or heterogeneous (Mohamed Eid et al., 2020; Azedou et al., 2023; Illán Fernández et al., 2024). Additionally, Gedle et al. (2024) reported an efficacy when applied during the growing season, because it allows separating bare soil from vegetation areas. To obtain the value of SAVI the following equation is used:

$$SAVI = \frac{NIR\ (B8) - Red\ (B4)}{NIR\ (B8) + Red\ (B4) + L} \cdot (1 + L) \quad (2)$$

Where L represents the correction factor with respect to the influence of soil brightness in areas with scarce vegetation, which its value varies from 0 to 1, with high values being high when there is scarce vegetation cover, while low values are suitable for dense vegetation. That said, in this study, an average value ($L = 0.5$) was chosen.

2.2.3 Normalized Difference Water Index (NDWI)

NDWI is applied for the detection and analysis of surface water, so it is usually useful in land cover studies to distinguish it from other classes (Haldar et al., 2023; Thepvongsa and Butar Butar, 2025). To obtain the value of NDWI, the following equation is applied (Gao, 1996):

$$NDWI = \frac{Green\ (B3) - NIR\ (B8)}{Green\ (B3) + NIR\ (B8)} \quad (3)$$

Where the values vary between -1 and +1, with positive values associated with water surfaces, while negative values or close to zero indicate another type of cover such as vegetation, bare soil or artificial surfaces.

2.2 Univariate image differencing (UID)

The UID is a type of change detection method proposed by Singh (1989), which evaluates variations in a spectral index of different dates, such as the evaluation of changes caused by extreme precipitation events (Chrysafi et al., 2025), identifying areas of loss or gain of a certain type of land cover.

In this work, the differences of the NDVI, SAVI and NDWI indices corresponding to pre- and post-Hanna were calculated from the following equation:

$$\Delta I = I_{pre} - I_{post} \quad (4)$$

where I represent the value of each spectral index, where positive values refer to a loss or decrease after the event, while negative values indicate an increase.

2.3 Change Vector Analysis (CVA)

The CVA allows quantifying the magnitude of the total impact, that is, considering the spectral changes of each index (Ansari et al., 2025). That said, this integral value allows us to detect in greater detail the areas where there was a greater post-Hanna spectral change. To calculate the total magnitude of the land cover change, a calculation of rasters was performed in GIS by applying a square root function with the values of the change of each index previously calculated, as expressed in the following equation:

$$CVA = \sqrt{\left(NDVI_{pre} - NDVI_{post}\right)^2 + (SAVI_{pre} - SAVI_{post})^2 + (NDWI_{pre} - NDWI_{post})^2} \quad (5)$$

Where the highest value obtained refers to areas with a greater magnitude of change in land cover, while the lowest values indicate that there was no change between the type of cover.

2.2 Land cover classification

A supervised land cover classification was performed in GEE using the RF algorithm implemented in JavaScript. RF has been widely applied for land cover mapping due to its robustness, ease of implementation, and high classification accuracy compared to traditional methods (Zhao et al., 2021; Svoboda et al., 2022; Macarringue et al., 2023).

The strata corresponded to the land cover classes defined in Table 2. A total of 296 points were selected, of which approximately 80% were used for training and 20% for independent validation, using the stratified random sampling method. The number of samples per class was allocated proportionally to the areal extent

of each class, in order to minimize sampling bias, distributed as follows: dense vegetation (53), medium vegetation (40), sparse vegetation (45), built-up (88), bare soil (55), water (15). While this sample size is lower than the commonly recommended upper range of 300-500 samples, RF performance has been found to be markedly improved by increasing training data to approximately 250-300 samples, while improvements in accuracy are typically minimal outside of that threshold (Bouasria et al., 2023).

The performance of the RF classifier was evaluated through confusion matrices and overall accuracy metrics computed separately for the pre-event and post-event classifications. This allowed a quantitative assessment of the reliability of the resulting land cover maps.

Land cover	Description	Differentiation criteria
Water bodies	Rivers, dams, canals, and permanent or temporary bodies of water	NDVI <0.0 and low reflectance in NIR
Bare soil	Areas without vegetation cover, eroded areas, or areas with exposed soil	NDVI between 0.0-0.1, high reflectance in red bands
Built-up area	Settlements, roads, industrial zones or buildings	Low NDVI <0.2, distinctive reflectance in visible light, identified mainly by training points
Dense vegetation	Dense tree cover or highly photosynthetically active vegetation	NDVI >0.45
Medium vegetation	Areas with intermediate, shrubby or transitional vegetation.	NDVI between 0.30-0.45
Sparse vegetation	Grasslands and scrublands with low green biomass density	NDVI between 0.10-0.30

Table 2. Description of land cover classes in the study area.

3. Results and Discussion

3.1 Land cover classification pre- and post-Hanna

Figures 3 and 4 show the pre- and post-Hanna classification results, where an increase from 35.39% to 44.77% in dense vegetation is highlighted, while medium vegetation increased from 22.29% to 35.37%. On the other hand, sparse vegetation presented a loss of 16.80% to 9.16%, which represents a net loss of -108.12 km^2. For the class of built-up area, there was also a reduction from 23.80% to 18.96&; while bare soil experienced a minor decrease of -0.63 km^2. The water bodies presented a small net gain of 1.12 km2. (Table 3).

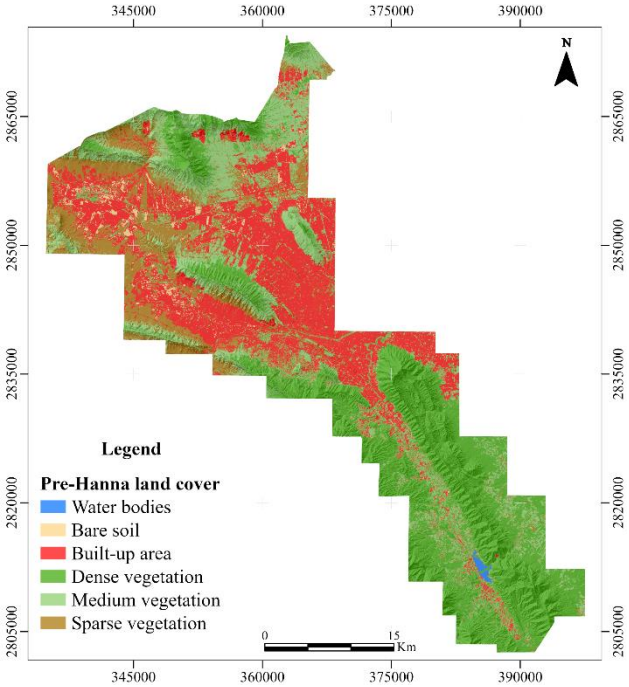

Figure 3. Pre-Hanna land cover classification map.

Therefore, the transition from less vigorous vegetation to more vigorous vegetation after the event is determined, consistent with the regrowth of vegetation, added to the response of extreme precipitation, this mainly observed along the slopes of the rock massifs and riparian corridors.

On the other hand, the apparent reduction of the built-up area can be attributed to a spectral misclassification effect; This may be due to the fact that wet surfaces and vegetation in peri-urban strips were classified as dense vegetation categories.

Land cover	Pre-Hanna area (Km^2)	%	Post-Hanna area (Km^2)	%	Change Area (Km^2)
Water bodies	3.9	0.28	6.95	0.49	3.05
Bare soil	24.25	1.71	28.87	2.04	4.62
Built-up area	377.16	26.67	270.39	19.11	-106.77
Dense vegetation	498.87	34.99	604.26	42.71	109.39
Medium vegetation	275.42	19.47	341.55	24.14	66.13
Sparse vegetation	238.79	16.88	162.88	11.51	-75.91

Table 3. Changes in land cover following Tropical Storm Hanna.

To assess the accuracy of land cover classification, confusion matrices were used starting from 20% of the points for validation. The pre-Hanna obtained an overall accuracy of 0.93 with a Kappa coefficient of 0.91. Table 4 shows that most of the classes obtained high reliability, however, an error was observed between bare soil and medium vegetation, as well as between built-up area and sparse vegetation; This may be due to the spectral similarity of these transition classes.

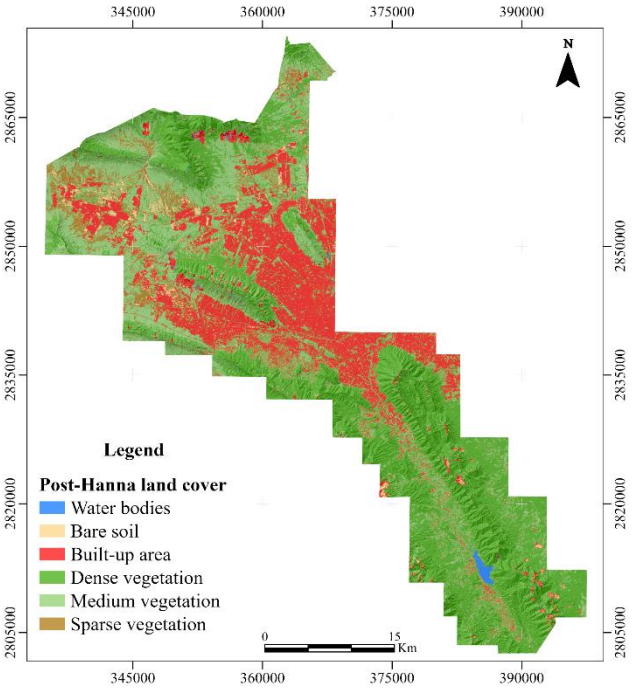

Figure 4. Post-Hanna land cover classification map.

With respect to the post-Hanna classification, the confusion matrix obtained an overall accuracy of 0.83 with a Kappa coefficient of 0.79. Table 5 shows a relatively high reliability, however, all classes presented minor errors, except for a notable misclassification of the medium vegetation class marked as sparse vegetation.

	Water bodies	Bare soil	Buil-up area	Dense vegetation	Medium vegetation	Sparse vegetation
Water bodies	3	0	0	0	0	0
Bare soil	0	9	0	0	1	0
Buil-up area	0	0	13	0	0	2
Dense vegetation	0	0	0	10	0	0
Medium vegetation	0	0	0	0	10	0
Sparse vegetation	0	0	1	0	0	9

Table 4. Pre-Hanna land cover classification confusion matrix.

	Water bodies	Bare soil	Buil-up area	Dense vegetation	Medium vegetation	Sparse vegetation
Water bodies	2	0	0	0	0	1
Bare soil	0	9	0	0	0	1
Buil-up area	0	0	14	0	0	1
Dense vegetation	0	1	0	8	0	1
Medium vegetation	0	0	0	0	6	4
Sparse vegetation	0	0	0	0	1	9

Table 5. Post-Hanna land cover classification confusion matrix.

In addition, the values of Producer's Accuracy (PA) and User's Accuracy (UA) were calculated for each coverage class (Table 6). For the Pre-Hanna classes, most classes showed high reliability, with PA values between 0.86 and 1.00 and AU values between 0.81 and 1.00, especially for water bodies, dense vegetation and built-up areas. In contrast, medium vegetation and sparse vegetation exhibit lower post-Hanna accuracy, probably due to soil moisture and transition in vegetation.

Land cover	PA	UA	PA	UA
Water bodies	1.00	1.00	0.66	1.00
Dense vegetation	1.00	1.00	0.88	1.00
Bare soil	0.86	0.92	0.93	1.00
Built-up area	0.90	1.00	0.90	0.90
Medium vegetation	1.00	0.90	0.60	0.85
Sparse vegetation	0.90	0.81	0.90	0.52

Table 6. Producer's Accuracy (PA) and User's Accuracy (UA) for each land cover class for pre- and post-Hanna.

While changes in coverage were quantified as area percentages, it is important to recognize that classification errors can influence the reported values. Although the general accuracy for pre- and post-Hanna (0.93 and 0.83, respectively) has obtained a good agreement, the variability in the metrics at the class level is notorious, specifically in the classes of medium vegetation and scattered vegetation (PA = 0.60 and AU = 0.52), so these uncertainties must be considered when interpreting the magnitude and spatial distribution of land cover transitions. Future studies could incorporate the error-adjusted area estimation framework proposed by Olofsson et al. (2014) to formally quantify uncertainty in estimates of change, especially when limited baseline data are available.

3.2 Index-based change detection

In a complementary analysis, change detection maps were generated for each spectral index. The ΔNDVI and ΔSAVI maps (Figures 5 and 6), show a general increase in vegetation greenness across the mountainous areas of medium elevation, particularly in the northern part of the study area. On the other hand, the high mountain areas presented high loss values, which indicates a loss of vegetation, probably related to mass removal processes or surface erosion caused by the event.

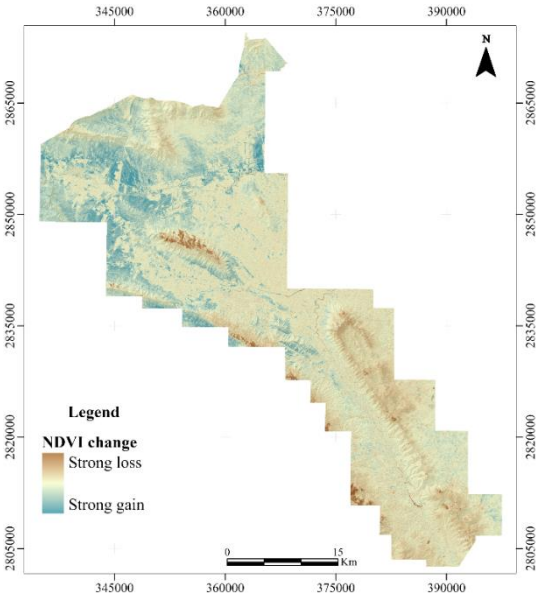

Figure 5. Change magnitude map for NDVI.

In contrast, the ΔNDWI change map (Figure 7) mostly shows a positive concentration along the post-Hanna river corridors, in addition to the temporary increase in soil moisture.

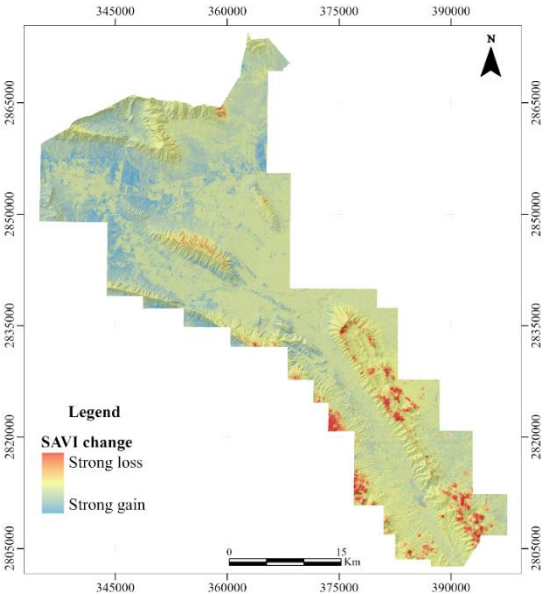

Figure 6. Change magnitude map for SAVI.

On the other hand, the negative changes of the NDWI were less extensive, occurring in fragmented patches along the mountain slopes, possibly related to the high slope and the infiltration or drying by the lithological conditions as observed in the center-east of the study area.

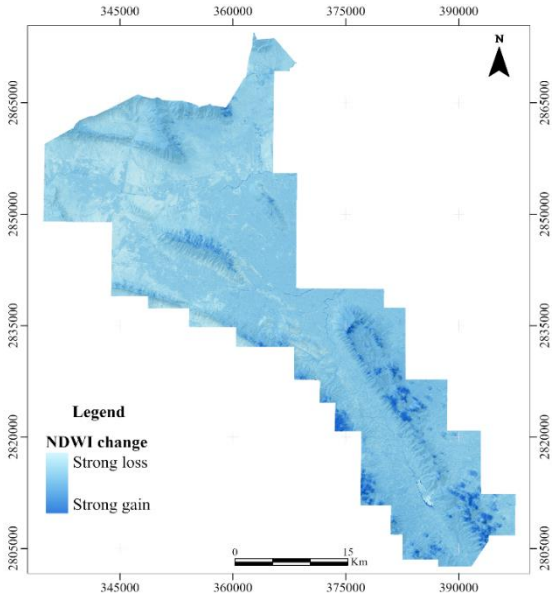

Figure 7. Change magnitude map for NDWI.

3.3 Multi-index CVA results

The CVA multi-index magnitude map (Figure 8) comprehensively represents the special distribution of post-Hanna spectral changes, where areas with significant alterations in vegetation cover and wet conditions are shown with higher values (dark red), while the lighter tones correspond to areas with minimal or no changes.

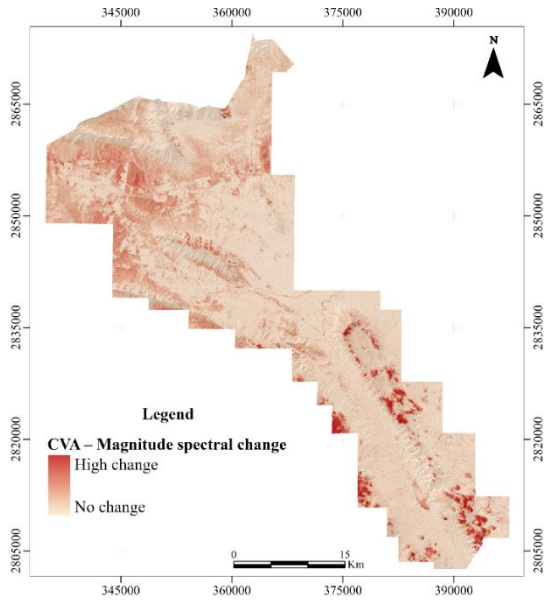

Figure 8. Multi-index magnitude map.

The high spectral magnitude change was concentrated along the mountain slopes and in specific areas of urban areas, particularly in the southern and central sectors of the study area, being consistent with the impacts expected after Tropical Storm Hanna, where vegetation cover may be reduced due to slope instability. surface runoff or temporary flooding. On the other hand, large sectors in the northern and flat urbanized areas exhibit low change, suggesting a more stable response to the event.

This contribution has been peer-reviewed. The double-blind peer-review was conducted on the basis of the full paper.
https://doi.org/10.5194/isprs-annals-X-3-W3-2025-11-2026 | © Author(s) 2026. CC BY 4.0 License.

4. Conclusion

This study demonstrates the applicability of integrating Sentinel-2 imagery with remote sensing techniques to assess land cover responses to extreme rainfall in an urban and mountainous environment. Using stratified random sampling, six land cover classes were determined through classification supervised with the RF algorithm, supported by NDVI, SAVI and NDWI. The pre- and post-Hanna models achieved overall accuracies of 0.93 and 0.83, with Kappa coefficients of 0.91 and 0.79, respectively, which demonstrates a good to high efficacy of the RF application for this type of studies.

Integrating these classifications with a multi-index CVA enabled the detection of both categorical and magnitude-based changes, determining significant vegetation disturbance and localized water dynamics after Tropical Storm Hanna (2020). The results highlight the dual effects of extreme precipitation: vegetation recovery in mid-elevation areas and degradation in erosion-prone slopes, together with increased surface moisture along riparian corridors. This multi-index approach provides a more nuanced understanding of short-term vegetation and hydrologic responses than any index alone.

Despite the strong performance of the methodology, some limitations should be acknowledged: (i) the analysis was based on only two temporal scenes, which restricts the interpretation of vegetation dynamics to a short-term window and may not fully capture longer recovery trajectories; (ii) spectral confusion between medium and sparse vegetation introduced uncertainty into post-event classification, as reflected in class-level accuracy metrics. Future studies could address these limitations by incorporating multi-temporal imagery, higher spatial resolution sensors, or additional spectral indices to improve vegetation separability. Overall, this proposed methodology offers a transferable framework for monitoring land cover dynamics in other urban mountain regions of the world in the face of extreme precipitation events.

Acknowledgements

The authors thank the Secretariat of Science, Humanities, Technology, and Innovation (Secihti) for awarding scholarships to Luis Arista (CVU: 1347829) and Kevin David Rodríguez (CVU: 1014573) through the Graduate Program of the Faculty of Civil Engineering—Master of Science in Environmental Engineering and Doctorate in Engineering with a focus on Environmental Engineering—at the Autonomous University of Nuevo León. We also acknowledge the Department of Geomatics at the Institute of Civil Engineering for providing the tools and resources necessary to carry out this research.

References

Abdo, H.G., Richi, S.M., 2024. Application of machine learning in the assessment of landslide susceptibility: A case study of mountainous eastern Mediterranean region, Syria. *Journal of King Saud University – Science*, 36(5), 103174. https://doi.org/10.1016/j.jksus.2024.103174.

Aguilar-Barajas, I., Sisto, N.P., Ramírez, A.I., Magaña-Rueda, V. 2019. Building urban resilience and knowledge co-production in the face of weather hazards: flash floods in the Monterrey Metropolitan Area (Mexico). *Environmental Science & Policy*, 99, 37-47. https://doi.org/10.1016/j.envsci.2019.05.021

Aguilar Durán, J.J., 2017. Modelo de evaluación del impacto de la precipitación sobre la inestabilidad de laderas en el Área Metropolitana de Monterrey, N.L. México. Master's tesis. Universidad Autónoma de Nuevo León.

Ansari, R.A., Esimaje, T., Ibrahim, O.M., Mulrooney, T., 2025. Analysis of Forest Change Detection Induced by Hurricane Helene Using Remote Sensing Data. *Forests*, 16, 788. https://doi.org/10.3390/f16050788

Azedou, A., Amine, A., Kisekka, I., Lahssini, S., Bouziani, Y., Moukrim, S., 2023. Enhancing Land Cover/Land Use (LCLU) classification through a comparative analysis of hyperparameters optimization approaches for deep neural network (DNN). *Ecological Informatics*, 78, 102333. https://doi.org/10.1016/j.ecoinf.2023.102333.

Bousria, A., Bouslihim, Y., Gupta, S., Taghizadeh-Mehrjardi, R., Hengl, T., 2023. Predictive performance of machine learning model with varying sampling designs, sample sizes, and spatial extents. *Ecological Informatics*, 78, 102294. https://doi.org/10.1016/j.ecoinf.2023.102294

Cabello, K.E., Germentil, M.Q., Blanco, A.C., Macatulad, E.G., Salmo III, S.G., 2021. Post-disaster assessment of mangrove forest recovery in Lawaan-Balangiga, eastern Samar using NDVI time series analysis. *ISPRS Ann. Photogramm. Remote Sens. Spatial Inf. Sci.*, 3, 243-250. https://doi.org/10.5194/isprs-annals-V-3-2021-243-2021.

Chen, L., Guo, Z., Yin, K., Shrestha, D.P., Jin, S. 2019., The influence of land use and land cover change on landslide susceptibility: a case study in Zhushan Town, Xuan'en County (Hubei, China). *Natural Hazard and Earth System Sciences*, 19(10), 2270–2228. https://doi.org/10.5194/nhess-19-2207-2019.

Chrysafi, A.-A., Tsangaratos, P., Ilia, I., Chen, W., 2025. Rapid Landslide Detection Following an Extreme Rainfall Event Using Remote Sensing Indices, Synthetic Aperture Radar Imagery, and Probabilistic Methods. *Land*, 14, 21. https://doi.org/10.3390/land14010021.

CONAGUA, 2020: Reseña del huracán "Hanna" del Océano Atlántico. (22 al 27 de julio de 2020). Comisión Nacional del Agua (CONAGUA). https://smn.conagua.gob.mx/tools/DATA/Ciclones%20Tropicales/Ciclones/2020-Hanna.pdf.

Di Napoli, M., Miele, P., Guerriero, L., Annibali-Corona, M., Calcaterra, D., Ramondini, M., Sellers, C., Di Martire, D., 2023. Multitemporal relative landslide exposure and risk analysis for the sustainable development of rapidly growing cities. *Landslides*, 20, 1781–1795. https://doi.org/10.1007/s10346-023-02065-z.

Froude, M.J., Petley, D.N., 2018. Global fatal landslide occurrence from 2004 to 2016. *Natural Hazard and Earth System Sciences*, 18(8), 2161-2181. https://doi.org/10.5194/nhess-18-2161-2018.

Gao, B.-C. 1996., NDWI—A normalized difference water index for remote sensing of vegetation liquid water from space. *Remote Sens. Environ*, 58(3), 257–266.

Gedle, A., Rientjes, T., Tamiru Haile, A., 2024. Integrating temporal-aggregated satellite image with multi-sensor image fusion for seasonal land-cover mapping of Shilansha watershed, rift valley basin of Ethiopia. *Remote Sensing Applications: Society and Environment*, 36, 101320. https://doi.org/10.1016/j.rsase.2024.101320.

Haldar, S., Mandal, S., Bhattacharya, S., Paul, S., 2023. Dynamicity of Land Use/Land Cover (LULC) An analysis from peri-urban and rural neighbourhoods of Durgapur Municipal Corporation (DMC) in India. *Regional Sustainability*, 4, 150-172. https://doi.org/10.1016/j.regsus.2023.05.001.

Huete, A.R., 1988. A soil-adjusted vegetation index (SAVI). *Remote Sensing of Environment. 25(3), 295-309.* https://doi.org/10.1016/0034-4257(88)90106-X.

Illán-Fernández, E.J., Tiede, D., Sudmanns, M., 2024. Consistent land use and land cover classification across 20 years of various high-resolution images for detecting soil sealing in Murcia, Spain. *Remote Sensing Applications: Society and Environment*, 35, 101223. https://doi.org/10.1016/j.rsase.2024.101223.

Isbaex, C., Coelho, A.M., 2021. The Potential of Sentinel-2 Satellite Images for Land Cover/Land-Use and Forest Biomass Estimation: A Review. *IntechOpen*. 10.5772/intechopen.93363.

Macarringue, L.S., Bolfe, É.L., Duverger, S.G., Sano, E.E., Caldas, M.M., Ferreira, M.C., Zullo Junior, J., Matias, L.F., 2023. Land Use and Land Cover Classification in the Northern Region of Mozambique Based on Landsat Time Series and Machine Learning. *ISPRS Int. J. Geo-Inf.*, 12(8), 342. https:// doi.org/10.3390/ijgi12080342.

Mohamed Eid, A.N., Olatubara, C.O., Ewemoje, T.A., El-Hennawy, M.T., Farouk, H., 2020. Inland wetland time-series digital change detection based on SAVI and NDWI indices: Wadi El-Rayan lakes, Egypt. *Remote Sensing Applications: Society and Environment*, 19, 100347. https://doi.org/10.1016/j.rsase.2020.100347.

Olofsson, P., Foody, G.M., Herold, M., Stehman, S.V., Woodcock, C.E., Wulder, M.A., 2014. Good practices for estimating area and assessing accuracy of land change. *Remote Sensing of Environment*, 148, 42-57. https://doi.org/10.1016/j.rse.2014.02.015

Pacheco Quevedo, R., Velastegui-Montoya, A., Montalván-Burbano, N., Morante-Carballo, F., Korup, O., Daleles Rennó, C., 2023. Land use and land cover as conditioning factor in landslide susceptibility: a literature review. *Landslides*, 20, p. 967-982. 10.1007/s10346-022-02020-4.

Padilla y Sánchez, R. J., 2007. Evolución geológica del sureste mexicano desde el Mesozoico al presente en el contexto regional del Golfo de México. *Boletín de la Sociedad Geológica Mexicana*, 59(1), 19-42.

Pereira, S., Santos, P.P., Zêzere, J.L., Tavares, A.O., García, R.A., Oliveira, S.C., 2020. A landslide risk index for municipal land use planning in Portugal. *Science of the Total Environment*, 735, 139463. https://doi.org/10.1016/j.ijdrr.2024.104264.

Promper, C., Puissant, A., Malet, J.P., Glade, T., 2014. Analysis of land cover changes in the past and the future as contribution to landslide risk scenarios. *Applied Geography*, 53, 11-19, 2014. https://doi.org/10.1016/j.apgeog.2014.05.020.

Rouse, J.W., Haas, R.H. Jr., Schell, J.A., Deergin, D.W., 1974. Monitoring vegetation systems in the Great Plains with ERTS. *NASA SP-351, Third ERTS-1 Symp.,* 1, Sect. A, 309-317.

SEDATU., 2024. Metrópolis de México 2020. Secretaría de Desarrollo Agrario, Territorial y Urbano. Gobierno de México. https://www.gob.mx/cms/uploads/sedatu/MM2020_06022024.pdf

Singh. A., 1989. Review article digital change detection techniques using remotely-sensed data. *Int. J. Remote Sens.*, 10(6), 989–1003. doi: 10.1080/01431168908903939.

Svoboda, J., Štych, P., Laštovička, J., Paluba, D., Kobliuk, N. 2022. Random Forest Classification of Land Use, Land-Use Change and Forestry (LULUCF) Using Sentinel-2 Data—A Case

Yepez Rincon, F., Lozano Garcia, D., Vela Coiffier, P., Rivera Rivera, L., 2013. Assessing hydrometeorological impacts with terrestrial and aerial Lidar data in Monterrey, México, *Int. Arch. Photogramm. Remote Sens. Spatial Inf. Sci*., XL-7/W2, 271–276, https://doi.org/10.5194/isprsarchives-XL-7-W2-271-2013